Journal of
Biomedical Optics

BiomedicalOptics.SPIEDigitalLibrary.org

Computed optical coherence microscopy of mouse brain *ex vivo*

Meiqi Wu
David M. Small
Nozomi Nishimura
Steven G. Adie

SPIE.

Meiqi Wu, David M. Small, Nozomi Nishimura, Steven G. Adie, "Computed optical coherence microscopy of mouse brain *ex vivo*," *J. Biomed. Opt.* **24**(11), 116002 (2019), doi: 10.1117/1.JBO.24.11.116002.

Journal of Biomedical Optics 24(11), 116002 (November 2019)

Computed optical coherence microscopy of mouse brain *ex vivo*

Meiqi Wu, David M. Small, Nozomi Nishimura, and Steven G. Adie*
Cornell University, Meinig School of Biomedical Engineering, Ithaca, New York, United States

Abstract. The compromise between lateral resolution and usable imaging depth range is a bottleneck for optical coherence tomography (OCT). Existing solutions for optical coherence microscopy (OCM) suffer from either large data size and long acquisition time or a nonideal point spread function. We present volumetric OCM of mouse brain *ex vivo* with a large depth coverage by leveraging computational adaptive optics (CAO) to significantly reduce the number of OCM volumes that need to be acquired with a Gaussian beam focused at different depths. We demonstrate volumetric reconstruction of *ex-vivo* mouse brain with lateral resolution of 2.2 μm, axial resolution of 4.7 μm, and depth range of ~1.2 mm optical path length, using only 11 OCT data volumes acquired on a spectral-domain OCM system. Compared to focus scanning with step size equal to the Rayleigh length of the beam, this is a factor of 4 fewer datasets required for volumetric imaging. Coregistered two-photon microscopy confirmed that CAO-OCM reconstructions can visualize various tissue microstructures in the brain. Our results also highlight the limitations of CAO in highly scattering media, particularly when attempting to reconstruct far from the focal plane or when imaging deep within the sample. [DOI: 10.1117/1.JBO.24.11.116002]

Keywords: optical coherence microscopy; computational adaptive optics; mouse brain.

Paper 190242R received Jul. 9, 2019; accepted for publication Oct. 18, 2019; published online Nov. 26, 2019.

1 Introduction

The basic science applications of optical coherence tomography (OCT) and optical coherence microscopy (OCM, the high-lateral-resolution version of OCT) are expanding, especially in the field of experimental neuroscience. Studies have revealed that OCM has the capability to visualize brain architecture and neural activity of rodents *in vivo*.[1–3] For example, optical coherence tractography using intrinsic scattering contrast can provide imaging and quantitative analysis of fibrous structures in the brain.[4] OCT has also been utilized to measure the refractive index of rat somatosensory cortex *in vivo*.[5]

As an interferometric imaging modality, OCT is sensitive to the complex optical field, containing both amplitude and phase (wavefront) information, which makes it well suited for computational postprocessing methods to restore the resolution in out-of-focus regions. Computational adaptive optics (CAO) can compensate for aberrations and defocus via a filtering operation in the transverse Fourier domain of the OCT data.[6,7] Moreover, it can also correct high-order aberrations without complex hardware adaptive optics.[8–11]

The compromise between lateral resolution and depth coverage represents a significant challenge for OCM to achieve large-volume imaging with cellular resolution. For example, in Srinivasan et al.,[1] a Gaussian beam focus was scanned in depth with a step of 5 μm, and only a small portion of OCM volumes acquired at each focus depth was extracted and synthesized into a composite volume combining high transverse resolution and signal-to-noise ratio (SNR), which results in large data size and long acquisition time. A number of methods have been demonstrated to alleviate this trade-off, including illumination with a nondiffracting Bessel beam[12,13] and numerical methods to compensate defocus.[6,8,14–17] However, these solutions either have nonideal side lobes in their point spread function or low SNR at out-of-focus depths. A combination of numerical methods and focus scanning has been proposed to generate volumetric reconstructions to combine high SNR and focal-plane transverse resolution and was demonstrated in a resolution phantom.[14] Here, we combine focus scanning[1,18,19] and CAO for high-resolution volumetric imaging deep in the scattering mouse brain. Using this method, only 11 OCT volumes acquired with focus planes 80 μm apart were required for imaging up to 1.2 mm optical path length (OPL) deep in the mouse brain with high spatial resolution. Two-photon microscopy (2PM) data was also taken to compare with OCM and CAO-OCM reconstructions.

2 Method

2.1 *Mouse Brain Preparation*

Mice heterozygous for Cx3Cr1-enhanced green fluorescent protein (GFP) [B6.129P(Cg)-Ptprca Cx3cr1tm1Litt/LittJ][20] and Thy1-yellow fluorescent protein (YFP) [B6.Cg-Tg(Thy1-YFP)HJrs/J],[21] with fluorescently labeled brain microglia and neurons, respectively, were used for experiments. Mice were intravenously injected with 100 μl Texas-Red lycopersicon esculentum lectin (Vector Labs TL-1176) 10 min prior to euthanasia to label brain vasculature. Euthanasia was induced by an intraperitoneal injection of pentobarbitol (150 μL of 39 mg/mL solution in saline) and then perfused via intracardiac puncture with 30-mL phosphate-buffered saline (PBS) containing 100 μl Texas-Red lectin at 4°C. The brain was harvested and then stored in PBS at 4°C, sealed in agarose (1%), and imaged within 1 h [Figs. 1(a), 1(b)]. Results from a single brain are reported in this paper, and two additional mice were used for method optimization.

---

*Address all correspondence to Steven G. Adie, E-mail: sga42@cornell.edu

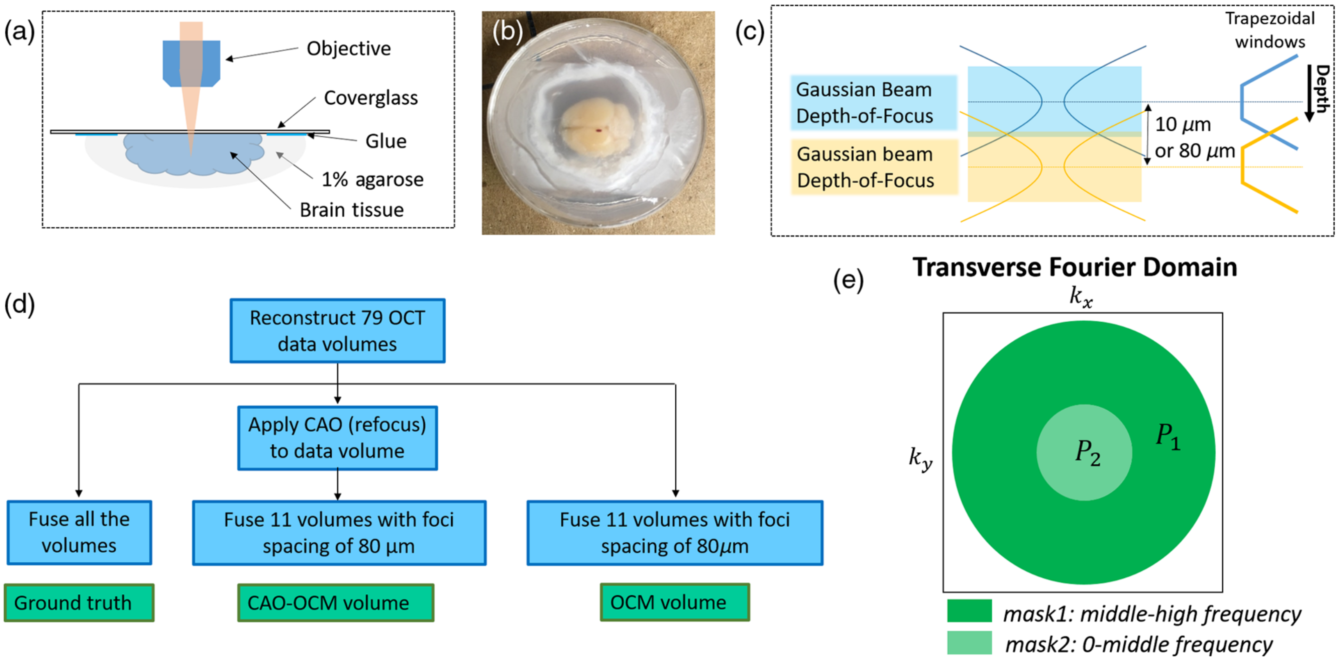

Fig. 1 Sample preparation and data processing. (a) Overview of sample geometry. (b) Photograph of sample. (c) Scheme of focus-scanning and fusion with trapezoidal window. Depth of focus is defined as twice the Rayleigh length of a Gaussian beam. (d) Flowchart of data processing. All the volumes acquired are reconstructed and fused with varying focus spacing. In this study, only defocus was corrected by CAO, and a frequency metric was used to search for optimal CAO coefficients. (e) Illustration of the frequency metric for CAO coefficient search.

2.2 *Optical Coherence Microscopy Imaging Protocol and Image Reconstruction*

Imaging was performed on a custom-built spectral-domain (SD)-OCM system, with a central wavelength of 1310 nm, with axial and transverse resolutions of 4.7 and 2.2 μm, respectively. The Rayleigh length of sample arm beam is 9 μm. A-scans were acquired at line rate of 30 kHz, B-scan frame rate of ∼25 Hz, and exposure time of 10 μs. Each acquired volume is composed of 1024×512 A-scans, corresponding to a transverse field of view (FOV) of 960 $\mu\mathrm{m} \times 480$ μm. The power applied to the sample was about 5 mW. The objective lens was LCPLN20XIR (Olympus). For the results presented in this work, 79 volumes were acquired with focus spacing of 10 μm, which is 1.11 Rayleigh lengths of the sample arm beam, by a stepper motor [KST101, Thorlabs, Fig. 1(c)]. For each dataset, subvolumes around the focus were extracted and synthesized[22] [by trapezoidal windows, Fig. 1(c)] together to form a new volume, which was upsampled and smoothed with a three-dimensional (3-D) median filter. The dimensions of the resultant volume were 960 $\mu\mathrm{m} \times 480$ $\mu\mathrm{m} \times 1200$ μm. A total of 11 OCM data volumes with focus separation of 80 μm were fused together to get the CAO-OCM and OCM volumes. Focus spacing of 80 μm was selected. More information on the factors that determined the selection of 80 μm can be found in Sec. 4.3.

All data processing was performed in MATLAB R2017a, Windows Server 2016 Standard. The raw spectral data were reconstructed following standard algorithms, including background subtraction, spectrum resampling, dispersion correction, and inverse Fourier transform. CAO-specific steps included focal plane curvature correction,[23] cover glass registration,[24] and demodulation.[23]

The standard OCM reconstruction (including background subtraction, spectrum resampling, dispersion correction, and inverse Fourier transform) took about 106 s for each data volume. Focal plane curvature calibration only needs to be done once and took about 110 s. Cover glass registration and demodulation took about 20 and 52 s, respectively, for each volume. The fusion of 79 volumes to generate “ground truth” took about 2175 s. The fusion of 11 volumes for OCM and CAO-OCM took about 220 s. The median filtering of ground truth, OCM, and CAO-OCM took about 223 s in total.

For each data volume, we took 90 to 110 planes near the focus to be a subvolume. We only optimized the correction of defocus for the subvolumes (i.e., we did not attempt to correct other optical aberrations). For each subvolume, it took about 150 s to optimize the refocus coefficients and 10 s to apply the correction.

2.3 *Two-Photon Microscopy and Optical Coherence Microscopy Coregistration*

A fiduciary mark was made on the cover glass and OCM and two-photon image volumes were acquired at a known distance and direction from the fiduciary. A 2PM was performed on a home-built system equipped with a Ti:sapphire laser (Chameleon Visionjh, Coherent) with the wavelength centered at 880 nm. A galvanometric scanner pair (Cambridge Technology) was used to perform an XY raster scan with the focus at a specified Z position at ∼1 frame/sec to generate a 512 pixel $\times 512$ pixel image. Lateral resolution was 0.5 μm and axial resolution was 3 μm. Emission was separated using a primary dichroic (705 nm); a secondary dichroic (520 nm); two tertiary dichroics (488 and 605 nm); and bandpass filters selective for Texas-Red (641/75), YFP (550/49), and GFP (517/65). Z-stack images were acquired using an Olympus XLPlan N 25× 1.05 NA objective, starting at the brain surface to 500 μm deep with 1-μm increments using a motorized linear stage DC motor (Newport). Laser scanning, data acquisition, and stage position were controlled by ScanImage software.[25]

2.4 *Computational Adaptive Optics*

In this study, CAO was only used to correct defocus. The computed pupil of OCT system can be modeled as an ideal pupil with an aberration phase factor:

$$H(Q_x, Q_y) = |H(Q_x, Q_y)|e^{i\varphi_{\text{aberration}}}, \tag{1}$$

where, Q_x and Q_y are the transverse angular spatial frequency coordinates, $|H(Q_x, Q_y)|$ is the ideal pupil, and $e^{i\varphi_{\text{aberration}}}$ is the aberration phase factor. CAO compensates the aberrated pupil via a phase filter:

$$H_{\text{AC}}(Q_x, Q_y) = H(Q_x, Q_y)e^{i\varphi_{\text{AC}}}, \tag{2}$$

where $H_{\text{AC}}(Q_x, Q_y)$ is the corrected pupil and $e^{i\varphi_{AC}} = e^{-i\varphi_{\text{aberration}}}$ is the phase filter. Since CAO was only used to correct defocus in this work, the phase filter is given as

$$\varphi_{\text{AC}} = \sqrt{(2k_c)^2 - Q_x^2 - Q_y^2}\,\Delta z, \tag{3}$$

where k_c is the central wavenumber (refractive index $n \times$ free-space wavenumber k_0) and Δz is the refocus coefficient (equal to $-1 \times$ displacement from focus). We first applied the estimated refocus coefficient and then fine-tuned it using an image metric as feedback.

2.5 *Image Quality Metric for Optimization of Computational Adaptive Optics Corrections*

The fine-tuning of refocus coefficient Δz were done by exhaustive search (Fig. 2) based on a metric that optimizes spatial frequency content, named as frequency metric. The metric is defined as the ratio of frequency energy within a middle-to-high range [P1 in Fig. 1(e)] of the transverse Fourier transform of the amplitude image to the energy within the middle frequency limit [P2 in Fig. 1(e)].[6] The frequency metric can be described by the following equation:

$$\frac{\sum\{|\text{FT}_{x,y}[|S(x,y,z)|]| * \text{mask1}\}^2}{\sum\{|\text{FT}_{x,y}[|S(x,y,z)|]| * \text{mask2}\}^2}, \tag{4}$$

where $\text{FT}_{x,y}$ is the Fourier transform in the transverse dimension and $S(x,y,z)$ is the corrected complex image. The choice of middle and high cut-off frequency, i.e., the boundaries of mask1 and mask2 in Fig. 1(e), will be discussed in Sec. 4.

Figure 2 shows how we found the optimal refocus coefficients based on the frequency metric. It demonstrates the exhaustive search of refocus coefficients for a volume with focus at about 124 μm OPL. Figure 2(a) is the optimal refocus coefficient found by frequency metric at each depth. Figures 2(c) and 2(d) show the frequency metric as a function of refocus coefficient for three planes at 44, 125, and 215 μm OPL depths,

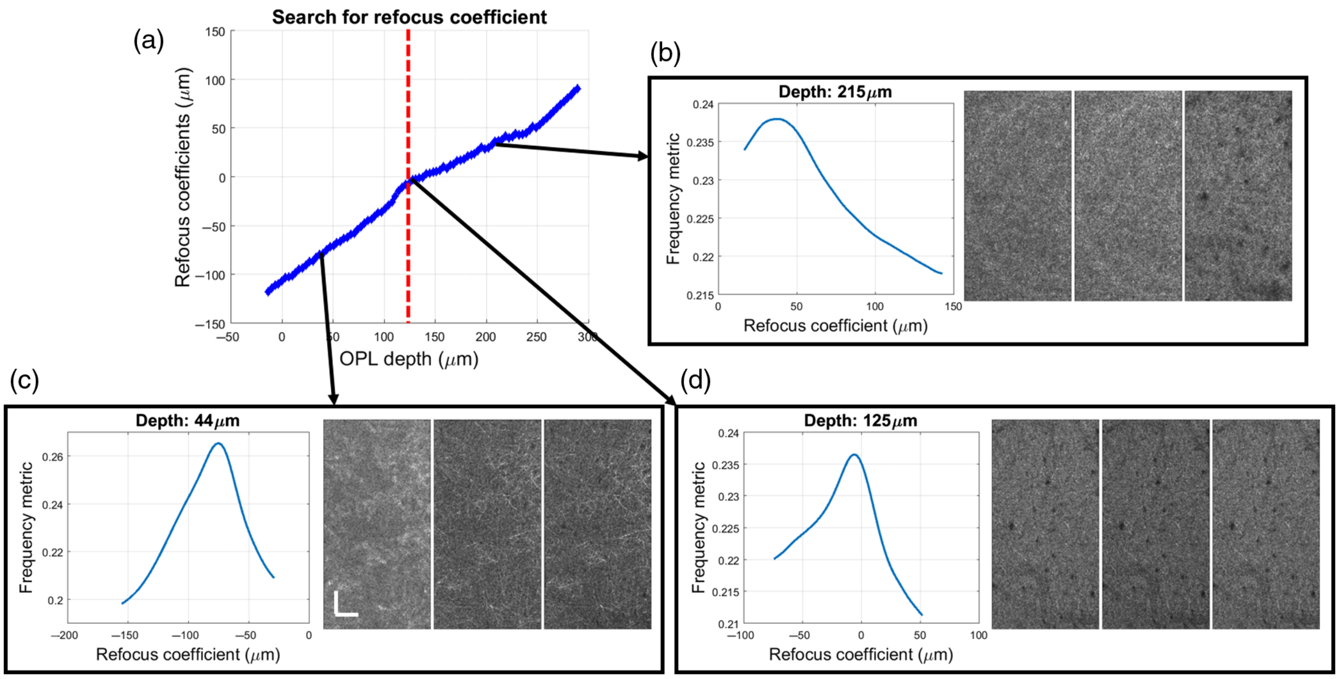

Fig. 2 Exhaustive search based on the frequency metric to find the optimal refocus coefficients for a volume with focus at about 124 μm OPL. (a) Optimal coefficients found by metric versus depth. Red vertical line indicates focus depth. (b)–(d) Frequency metrics versus refocus coefficients that were calculated at each depth (indicated by arrows) and used to identify the optimal value. The corresponding *en-face* planes (left: OCM, middle: CAO-OCM with optimal coefficients found by metric, right: at-focus ground truth) are also included. Gamma correction was applied to the images with $\gamma = 0.7$. Scale bar = 100 μm.

respectively. Video versions of Fig. 2(b)—2(d) can be found in Videos 1–3, respectively. With constant refractive index, the refocus coefficients are expected to be linear with depth. Linear fitting was applied to the optimal refocus coefficients founded by metric. Considering the depth-dependent refractive index in the biological tissue, a tolerance of 18.2 μm was allowed, compared to the linear fitting. For one plane, if the searched coefficient was within the fitted value of ±18.2 μm, the searched coefficient was used for correction, otherwise the fitted value was used.

2.6 *Normalization and Fusion Procedures*

The data volumes are synthesized into a new volume using a trapezoidal window [Fig. 1(c)], following the procedure outlined in the so-called Gabor fusion technique.[22] Because of large focus spacing, a larger window is used to fuse CAO-OCM and OCM than at-focus ground truth.

Before fusion, we divided the data volume by the 98th percentile of each plane to normalize the high signal level in the near-focus regions. After fusion, to reduce the banding artifacts along depth caused by low SNR in the out-of-focus regions, we subtracted the synthesized volume by the second percentile of each plane.

2.7 *Signal-to-Background Ratio Estimation*

The estimation of signal-to-background ratio (SBR) is based on the assumption that background level is uniformly distributed in the transverse Fourier domain, and there is no signal component but only background in the high frequency range. First, we normalized the transverse frequency range from 0 to 1. Then, we calculated the background energy density in the high frequency range (i.e., 0.95 to 1). By multiplying the background energy density and the spatial domain area of the frequency range we are interested in, we got the background energy level in that frequency range. Therefore, by subtracting the background energy level from the total energy level, we got the signal energy level in that frequency range.

3 Results

3.1 *Comparison of Optical Coherence Microscopy and Computational Adaptive Optics-Optical Coherence Microscopy with Two-Photon Microscopy*

OCM volumes from a region in cortex of the extracted mouse brain, acquired with focus spacing of 10 μm, were fused into a synthetic volume using previously developed methods[22] to generate an at-focus ground truth image. To verify the ability of OCM and CAO-OCM with larger focus spacing to resolve small brain structures, 2PM data in the same location were taken immediately after OCT scanning and compared with fused OCM and CAO-OCM (Fig. 3). Because of low backscattering, cell bodies and vessels manifest themselves as dark regions in OCM. Therefore, we utilize minimum intensity projection (MinIP) to highlight those structures in OCM.[1] Similarly, neurites (dendrites and myelinated axons) manifest themselves as bright regions in OCM,[1] so following Srinivasan et al.[1] we utilized a maximum intensity projection (MaxIP) to highlight these structures. MaxIP of 2PM data in the same volume show fluorescently labeled blood vessels, neural dendrites, and microglia. As indicated in Fig. 2, some of the same structures were found in CAO-OCM and 2PM images and included both cell bodies and microvessels.

3.2 *Volumetric Computational Adaptive Optics-Optical Coherence Microscopy of Fresh* Ex Vivo *Mouse Brain*

With beam Rayleigh length of 9 μm, focus scanning with step of 80 μm results in a factor of 4 fewer datasets, compared to focusing scanning with step equal to twice the Rayleigh length. Figures 4 and 5 show planes extracted from volumetric reconstructions of *ex vivo* mouse brain tissue. Four *en-face* planes, at optical depths of 83, 556, 914, and 1150 μm in the tissue (Fig. 4), and one cross section (Fig. 5) are extracted from the volume. Figure 4 displays comparisons of each plane with and without CAO. Fibrous structures can clearly be seen in the upper ~100 μm [Fig. 4(a)], consistent with the network of myelinated axons and dendrites found in layer 1 of the cortex. Thicker fibers

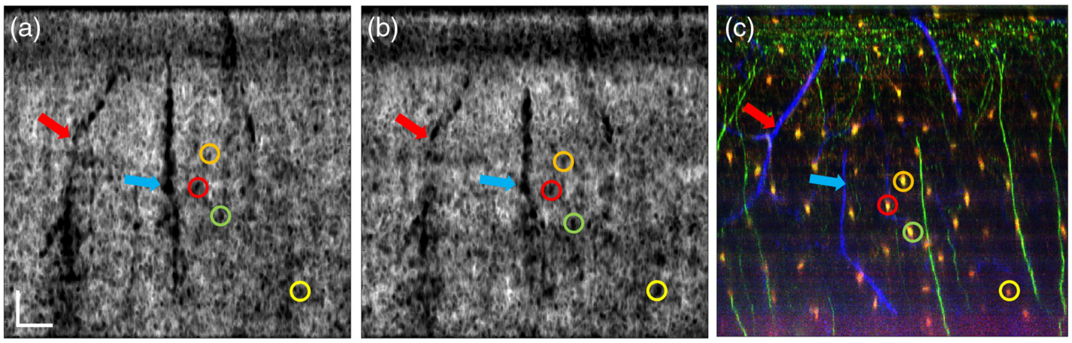

Fig. 3 Comparison of microstructure observable with fused ground-truth OCM (fusion of datasets taken with 10-μm focus spacing), fused CAO-OCM (fusion of datasets taken with 80-μm focus spacing), and 2PM. Vessels are indicated by arrows and cell bodies are indicated by circles. (a) MinIP of cross-sectional OCM images (MinIP taken over 46 μm along the slow scan axis of 3-D OCM dataset). (b) MinIP of cross-sectional CAO-OCM images (MinIP taken over 46 μm along the slow scan axis of 3-D CAO-OCM dataset). (c) MaxIP of 2PM data (over 42 μm), where blue indicates vessel (Texas-Red lectin), green indicates neurons (YFP), and yellow/red indicates microglia (GFP). Scale bar = 50 μm. Note that the depth range of the cross-sectional OCM and CAOOCM images have been cropped to match the depth range of the 2PM image.

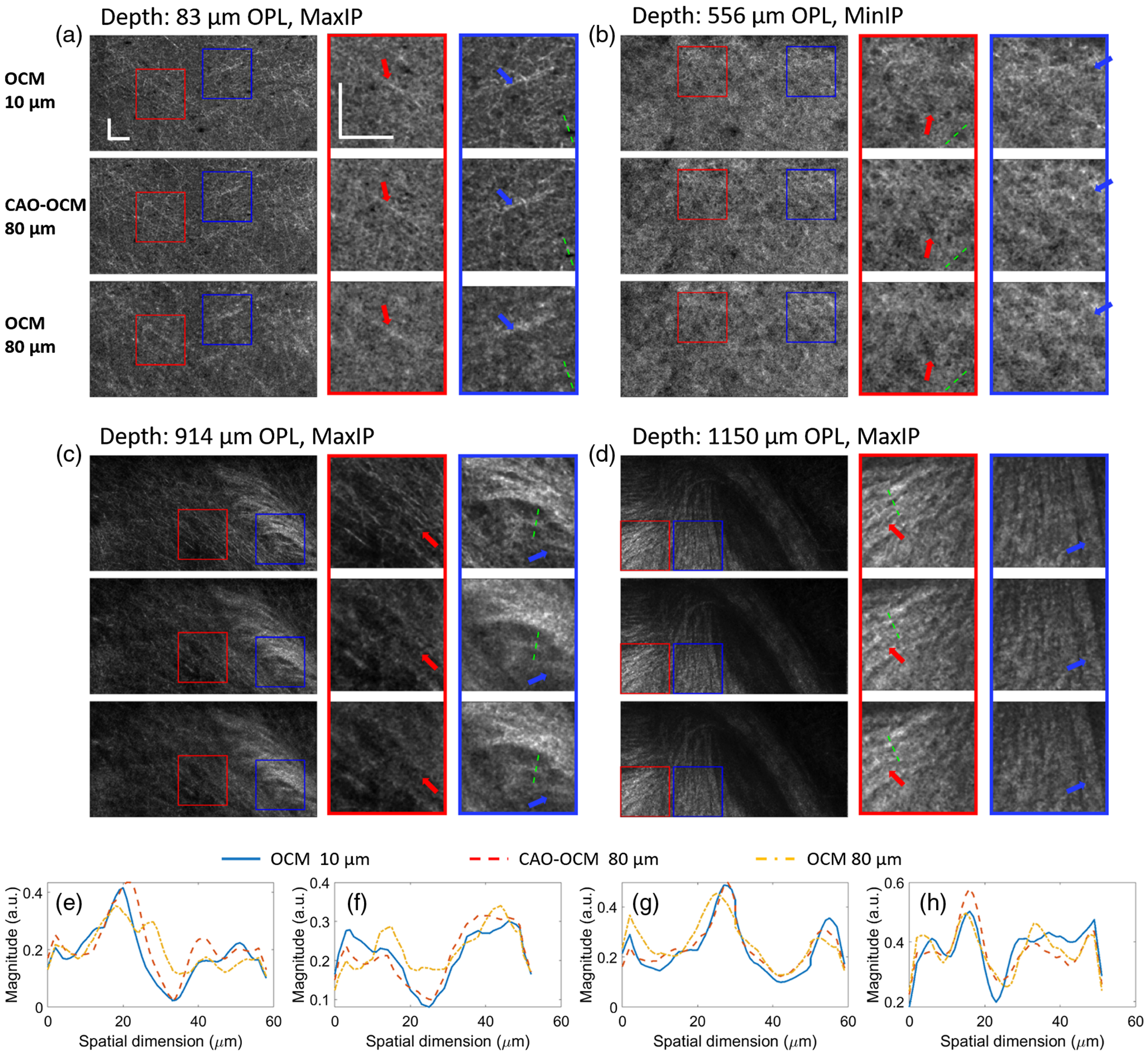

Fig. 4 Comparison of selected *en-face* planes from OCM ground truth reconstructed with dense (10 μm) focus spacing, and CAO-OCM and OCM reconstructed with sparse (80 μm) focus spacing at optical depths of (a) 83 μm (68 μm to shallower focus, 53 μm to deeper focus, MaxIP over 8 μm along depth), (b) 556 μm (63 μm to shallower focus, 58 μm to deeper focus, MinIP over 8 μm along depth), (c) 914 μm (61 μm to shallower focus, 60 μm to deeper focus, MaxIP over 8 μm along depth), and (d) 1150 μm (58 μm to shallower focus, 20 μm to deeper focus, MaxIP over 8 μm along depth). For (a)–(d), the first row shows fused OCM with 10-μm focus spacing (ground truth), the second row shows fused CAO-OCM with 80-μm focus spacing, and the third row shows fused OCM with 80-μm focus spacing; (a)–(d) also contain zoomed-in figures with red or blue margins. (e)–(h) Line plots of magnitude along the green dashed lines in the zoomed images in (a)–(d), respectively. Blue curves are fused OCM with 10-μm focus spacing, red curves are fused CAO-OCM with 80-μm focus spacing, and yellow curves are fused OCM with 80-μm focus spacing. Microstructures can be visualized more clearly in CAO-OCM than OCM [myelinated axons indicated by red and blue arrows in (a), cell body indicated by red arrows in (b), and fibers indicated by blue arrows in (c)]. When approaching (d) 1150 μm deep, CAO no longer provides any obvious improvement. Scale bar = 100 μm.

at ~1000 μm in depth with parallel orientations [Fig. 4(d)] are consistent with myelinated axons found in white matter.[26,27] Fly-through of *en-face* planes from ground truth, CAO-OCM, and OCM are contained in Video 13.

In the zoomed-in panels in Figs. 4 and 5, microstructures can be visualized more clearly in CAO-OCM than OCM. However, when getting deep in the tissue, the improvement provided by CAO is not as evident as at shallower depths. This is evident from the line plots [Figs. 4(e)–4(g)], where the curves from CAO-OCM have better similarity to the ground truth than OCM without correction by CAO. Furthermore, CAO-OCM makes the cell bodies darker [Figs. 4(e)–4(f)] and the defocused fiber narrower [Fig. 4(g), Video 1]. However, as it gets deeper in the tissue, CAO does not provide much improvement to OCM

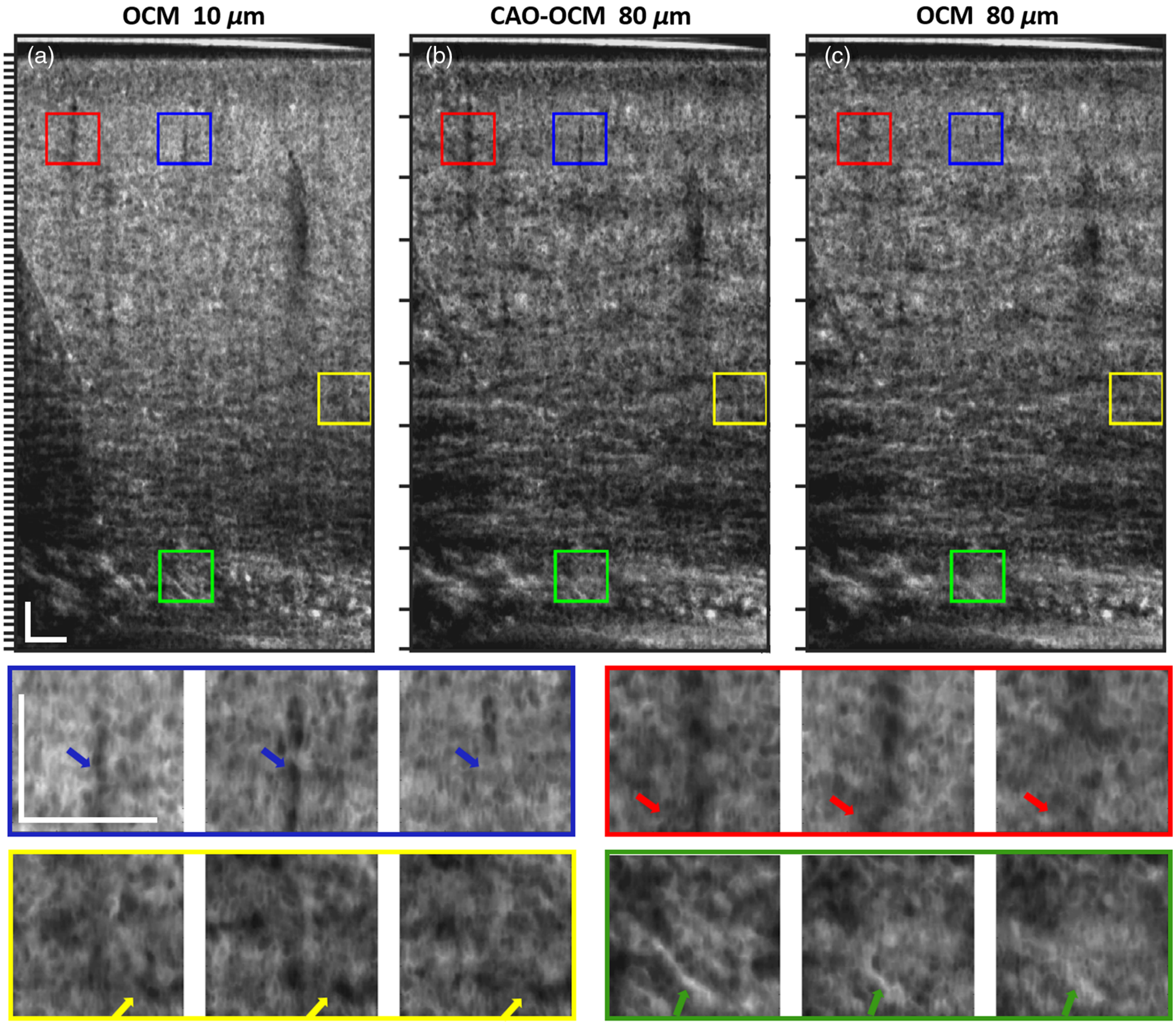

Fig. 5 Cross sections extracted from volumetric reconstructions of mouse brain (MinIP taken over 22 μm along the slow scan axis of 3-D OCM dataset). (a) Fused OCM with 10-μm focus spacing (ground truth), (b) fused CAO-OCM with 80-μm focus spacing, and (c) fused OCM with 80-μm focus spacing. The bottom two rows show zoomed-in images of the boxes in (a)–(c). Ticks on the vertical axis indicate the relative depths of foci of single OCM volumes that constitute the fused volumes. Microstructures can be visualized more clearly in CAO-OCM than OCM (e.g., the cell body indicated by yellow arrows, microvessels indicated by blue and red arrows, fibers indicated by green arrows in the zoom-in figures). Scale bar = 100 μm.

[Figs. 4(d), 4(h), Video 12]. The limitations of CAO in scattering tissue will be discussed in Sec. 4.

4 Discussion

4.1 *Choice of Image Metric for Optimizing Computational Adaptive Optics Corrections*

Previous studies have shown the applications of intensity-based metrics for numerical correction of OCT data, i.e., sharpness metric,[28,29] entropy metric,[30,31] and etc. For images with point-like (sharp) features, the intensity-based metrics can easily capture the increasing constructive interference as aberrations are minimized, because the intensity of point-like objects increases with constructive interference. However, in scattering samples without distinct structures, the intensity-based metrics could be disrupted by the ubiquitous speckles. Therefore, we chose a frequency-based metric, which is based on the assumption that middle-to-high frequency components of OCM or CAO-OCM magnitude images increases as the resolution improves (when the aberrations are minimized).[6]

4.2 *Choice of Middle and High Cut-off Values for Frequency Metric*

As is mentioned in Sec. 2, we utilized a frequency metric to provide feedback for CAO coefficient search. This is defined as the ratio of frequency energy within a middle–high range [P1 in Fig. 1(e)] of the transverse Fourier transform of the magnitude of each *en-face* OCM image to the energy within the middle frequency limit [P2 in Fig. 1(e)].[6] The middle and high cut-off frequencies could affect the performance of this metric. Therefore, the choice of middle and high cut-off frequencies is critical.

To choose these cut-off frequencies, we need to identify the transverse frequency components that are most sensitive to defocus. We randomly chose three at-focus planes at depth of 94, 513, and 932 μm OPL as reference depths [Fig. 6(a)]. For each reference depth, we found the defocused version from the original focus-scanning dataset acquired with step of 10 μm [Fig. 6(a)]. Figure 6 demonstrates a defocused version of the reference at 94 μm OPL depth. The defocused plane is 168 μm OPL above the focus. Figures 6(b) and 6(c) show the reference and defocused versions, respectively. Figure 6(c) is the difference between spectrum energy of the magnitude of reference and defocused version (in decibel scale), whose total energies are both normalized to 1. To more clearly visualize the spectrum energy difference, we transformed the two-dimensional spectrum energy into a one-dimensional vector along the normalized transverse spatial frequency radius axis Q_r and plotted in Fig. 6(d). From Fig. 6, we found the frequency range where the defocused version generally has lower energy than the reference, and then chose the frequency range limits as the middle and high cut-off frequencies. The cut-off frequencies that we used to calculate the frequency metric are indicated by green dash lines in Fig. 6(d) and green dash circles in Fig. 6(c). Video 4 contains additional information of more defocused versions with respect to reference at 94 μm OPL depth. The same procedure was also applied to references at 513 and 932 μm OPL depths. The results can be found in Videos 5 and 6, respectively.

To investigate the sensitivity of the image metric to the choice of cut-off frequencies, we plotted the optimal coefficient

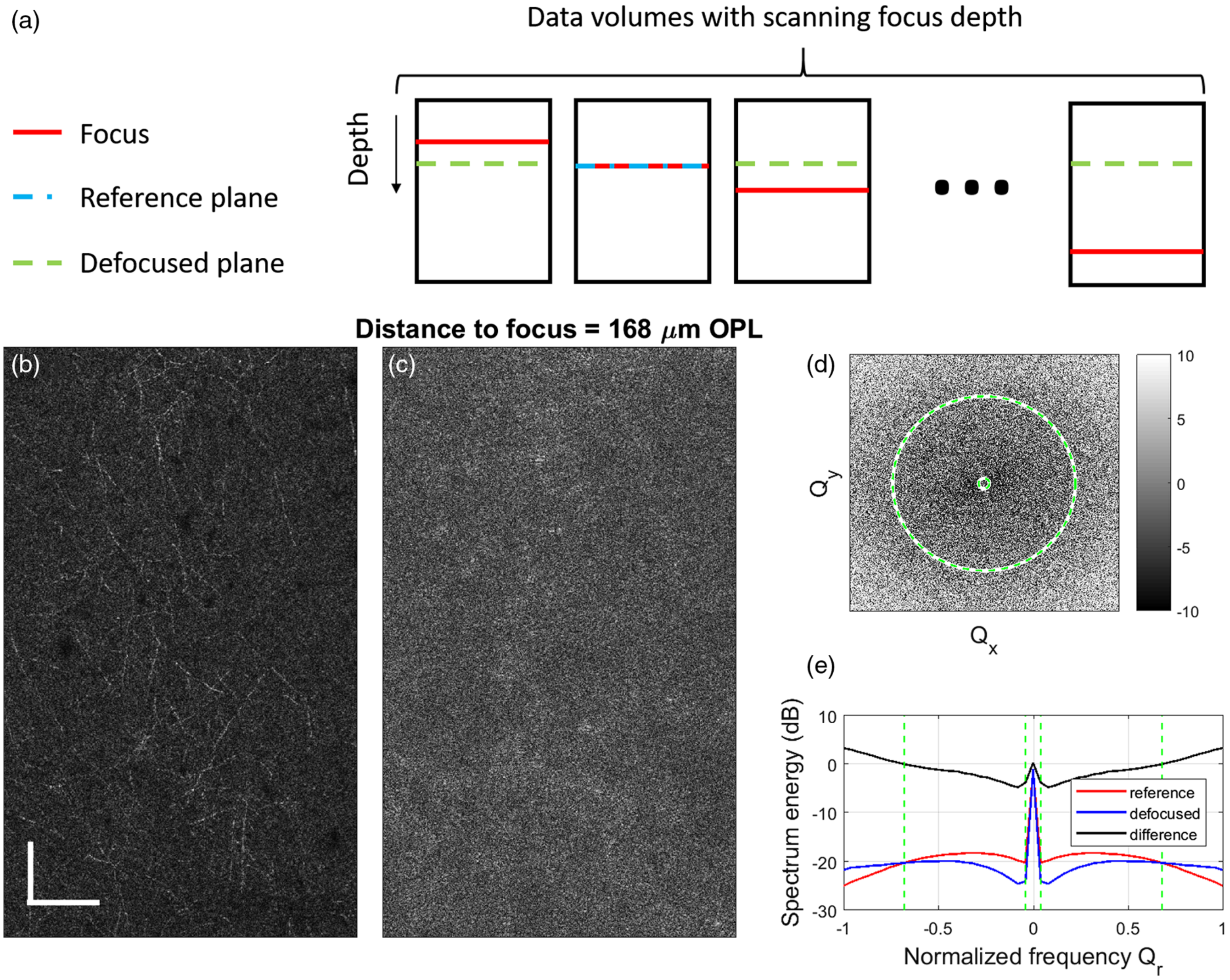

Fig. 6 Variations in transverse spectrum energy distribution of physically defocused images. (a) Scheme to demonstrate how we chose the references and their defocused version. (b) At-focus reference at 94 μm OPL depth and (b) its defocused version, which is 168 μm above the focus (positive distance indicates depth above the focus, and negative distance indicates depth below the focus). (d) Difference between spectrum energy of the magnitude of reference and defocused version (in decibel scale). Here Q_x and Q_y are the transverse spatial frequency coordinates. (e) Plot of spectrum energy of magnitude of reference and defocus version, and the difference between them (defocused version minus reference), along normalized frequency radius axis Q_r. Green dash lines and green circles in (c) and (d) indicate the cut-off frequencies used for calculating metrics. Gamma correction was applied to the images with $\gamma = 0.7$. Scale bar $=$ 100 μm.

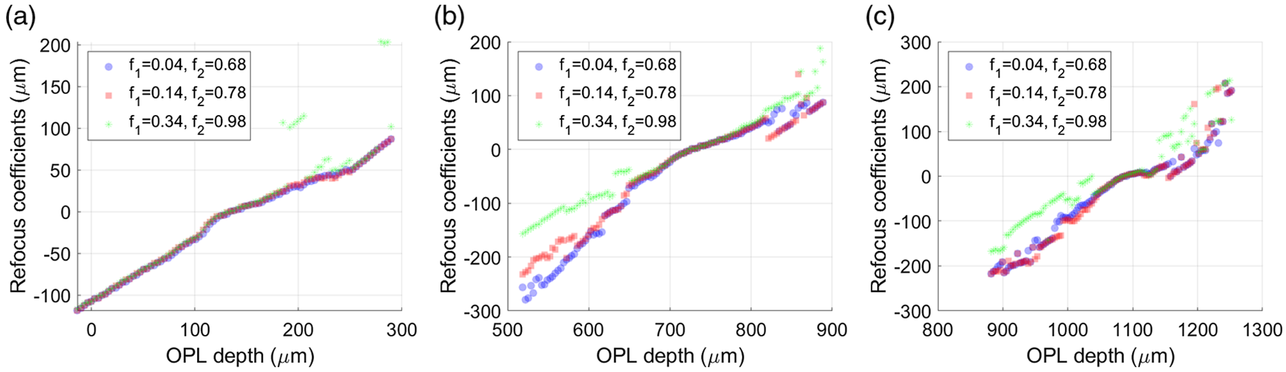

Fig. 7 Plot of the optimal refocus coefficient found by metrics with different cut-off frequencies, for three volumes with focus at (a) 124, (b) 722, and (c) 1085 μm.

found by metrics with different mask sizes in Fig. 7. The values of f_1 and f_2 correspond to the middle and high cut-off frequencies, respectively. In this paper, we used $f_1 = 0.04$ and $f_2 = 0.68$. We found that, for data volume with shallow focus [Fig. 7(a)], CAO is less sensitive to the choice of f_1 and f_2, whereas for data volume with deeper focus [Fig. 7(c)], CAO is more sensitive to the choice of f_1 and f_2, particularly when further away from the focus. This is consistent with our discussion about limitations of CAO in Sec. 4.4. For the depth range we used for fusion, the metric is insensitive to the choice of f_1 and f_2 within variance up to 0.2.

4.3 Determining Appropriate Focus Spacing for Large-Scale Volumetric Computational Adaptive Optics-Optical Coherence Microscopy

In a Gaussian-beam imaging system, signal strength decreases with distance from focus because of confocal gating. The rate of signal decay with distance from focus increases with the numerical aperture of the system, which reduces the depth range over which the signal is above the OCT system noise floor. Therefore, the "usable depth range" of CAO-OCM depends on both the numerical aperture of the confocal gate and the dynamic range of the OCT system.[32]

In a highly scattering biological sample, the usable depth range is further reduced by multiple scattering and "cross talk"[33–35] (see Sec. 4.4, for further discussion). Moreover, CAO does not solve the signal loss in the scattering tissue sample. We cannot apply CAO in a single-acquired OCM volume to reconstruct with high resolution and SNR throughout a large depth range. For this reason, focus scanning is required. This leads to a trade-off between resolution and number of required focus-scanned OCT volumes (or the maximum distance between focus positions). The focus spacing is governed by the decay in collected signal with distance from the focus, and the level of scattering of the sample. In this work, we chose 80 μm as the focus spacing for CAO-OCM, because CAO works reasonably well (visually showed similar tissue microstructure to the ground truth) in this setting but not with focus spacing of 100 μm or more (see Videos 1–3, for shallow depth in the sample; Videos 7–9, for moderate depth in the sample; and Videos 10–12, for deep in the sample). CAO-OCM with focus separation of 80 μm provided enabled visualization of tissue microstructures such as dendrites or myelinated axons, cell bodies, and vessels. These microstructures were more clearly visualized than in a CAO-OCM volume fused with 160-μm focus spacing. (The depth-dependent image metric of 160-μm focus spacing also indicated lower image quality—data not shown.) We note that the selection of 80-μm focus spacing was not a result of an optimization process, and so further work is needed to determine the focus separation that minimizes the number of required volumes without compromising CAO-reconstructed image quality too much. Considering the depth-dependent OCT image quality and performance of CAO in any given sample, a nonuniform focus separation may be considered in a future study.

4.4 Limitations of Computational Imaging in Scattering Tissues

Figure 8 is generated to investigate the limitations of CAO in scattering tissues. Figures 8(a) and 8(b) demonstrate exhaustive search of refocus coefficients for volumes with focus at about 722 and 1082 μm OPL, respectively. For planes away from the focus, the search of coefficients is less convex than those closer to the focus (Figs. 2, 8(a), and 8(b)]. Furthermore, from the *en-face* planes in Videos 1–3 and 7–12, CAO cannot provide obvious improvement to planes away from the focus, especially deep in the tissue. This could be due to the reduction of SBR as distance from the focus increases. Figure 8(c) is the plot of SBR versus depth for the volumes in Figs. 8(a) and 8(b). The SBR is higher for planes closer to the focus, and the volume with deeper focal depths has lower SBR.

Figure 9 shows the frequency metric and normalized contrast versus depth in the synthetic volumes. The fluctuation in frequency metric of OCM with 80-μm focus spacing is due to defocus. After CAO correction, the fluctuation still exists but does show some improvement over OCM. The normalized contrast for each depth was calculated from a subvolume (five planes centered about the given depth) by subtracting the 20th percentile of the OCT signal magnitude from the 95th percentile and then dividing by the median signal of the subvolume. The normalized contrast curves show similar fluctuations to frequency metric curves, except the increasing trend deeper in the sample. The increasing contrast for depths in the 800 to 1200 μm range is likely due to the high-scattering regions of white matter tissue, which contrasts with other relatively low-scattering regions within the transverse FOV (see Video 13).

The improvement provided by CAO is less obvious for deeper planes (Fig. 9 and Video 13). The frequency curves show that CAO correction in scattering brain tissue cannot restore all the frequency content obtained with ground-truth focal plane imaging. This suggests that the performance of CAO depends on SBR, which includes the effect of single-to-multiple

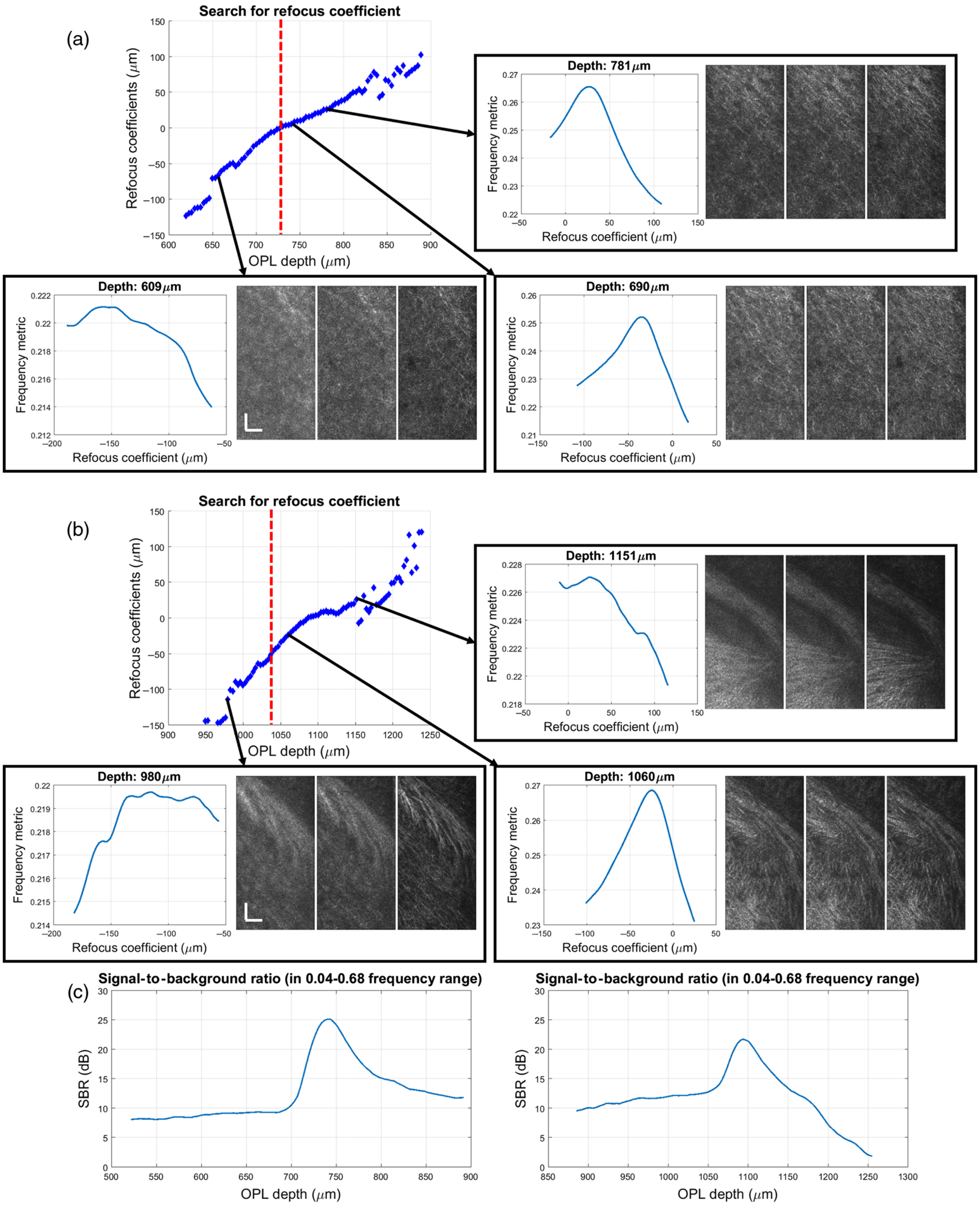

Fig. 8 Limitations of CAO in the scattering tissue. (a) and (b) Exhaustive search of optimal refocus coefficients for volumes with focus at about 722 and 1082 μm OPL, respectively. In (a) and (b), the top-left figures are plots of optimal refocus coefficients found maximizing the frequency metric at each depth. Red vertical line indicates focus depth. The boxed figures are examples of frequency metrics versus refocus coefficients that were calculated at each depth (indicated by arrows) and used to identify the optimal value. The corresponding *en-face* planes (left: OCM, middle: CAO-OCM with optimal coefficients found by metric, right: at-focus ground truth) are also included. The video versions of the boxed figures can be found in Videos 7–12. (c) SBR for the volumes in (a) and (b). Gamma correction was applied to the images with $\gamma = 0.7$. Scale bar = 100 μm.

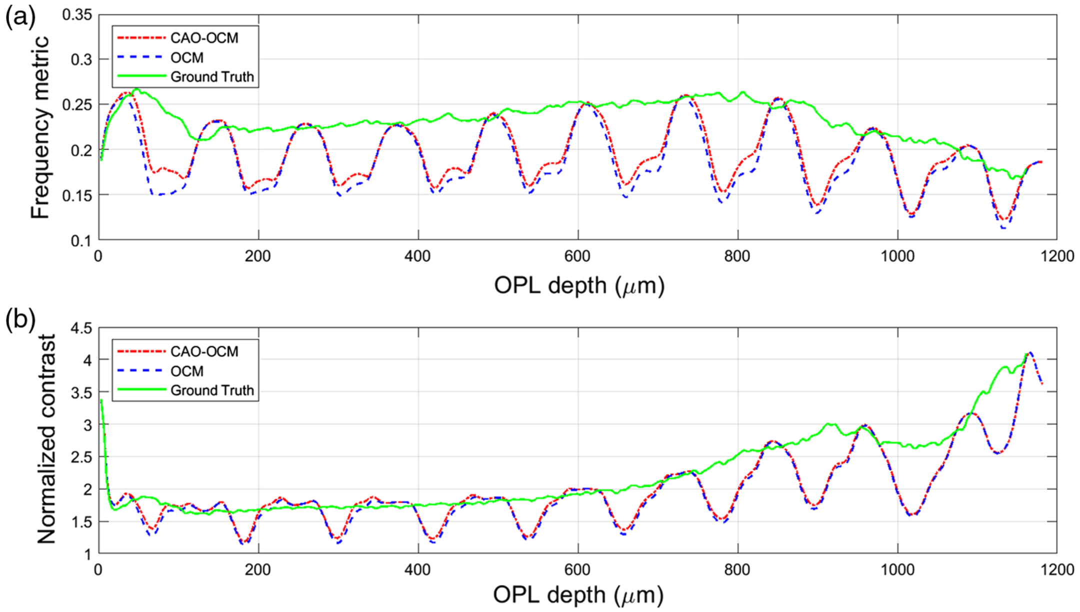

Fig. 9 Quantitative analysis of depth-dependent image quality for the synthetic volumes of CAO-OCM, OCM, and ground truth. (a) Frequency metric and (b) normalized contrast (see text for definition).

scattering ratio[36] and SNR. An unexpected contribution to the multiple scattering background could arise from the phenomenon of cross talk.[33–35] Although cross talk is traditionally associated with full-field OCT approaches that use spatially coherent illumination, we note that when reconstructing away-from-focus, these depths are illuminated by spatially coherent light over an extended area (governed by the Gaussian beam diameter at that depth). Because of multiple scattering, the usable depth range in mouse brain (~100 μm) is much shorter than low-scattering cell culture (~500 μm).[32] Low SNR and multiple scattering in deep tissue can limit the ability of CAO to reconstruct accurate, high-resolution sample structure. Fortunately, techniques exist to overcome the limitation caused by multiple scattering, for example, through optical tissue clearing,[37] which are applicable to *ex-vivo* imaging of tissues.

4.5 *Importance of Phase Stability for Computational Adaptive Optics-Optical Coherence Microscopy*

Phase-dependent postprocessing techniques, including CAO and interferometric synthetic aperture microscopy, are sensitive to phase stability.[38] In previous research, an experiment of localized disturbance on an SD-OCT system demonstrated the depth-dependent phase stability requirements.[39] Owing to the expansion of a Gaussian imaging beam with increasing distance from focus, the depths far from the focus experience a longer interrogation time (the dwell time of the Gaussian beam at a given location during XY raster scanning), compared to the depths near the focus. As a result, computational correction of depths far from the focus requires higher phase stability.

In this paper, cover glass phase registration[24] was employed to improve the phase stability in the sample. This method of phase registration was sufficient for *ex-vivo* imaging. However, for *in-vivo* imaging in mouse brain, further techniques may be required to solve the phase instability issue caused by tissue motion. Several methods have been reported for 3-D motion correction. For *in-vivo* skin imaging, motion along the optical axis was corrected using phase differences between A-scans, and motion orthogonal to the optical axis was corrected utilizing a speckle-tracking system.[40] In the retinal CAO imaging, the effect of motion was mitigated through a combination of high-speed acquisition and postacquisition phase correction.[9]

5 Conclusion

We have demonstrated that CAO can improve the resolution at planes distant from the focus in fresh *ex-vivo* mouse brain. In this work, a volumetric image of mouse brain with cellular resolution and depth range of 1.2 mm OPL was reconstructed. Various structures can be visualized by CAO-OCM reconstructions, including branching microstructure associated with neural networks in layer 1 of the cortex, myelinated axons in white matter, cell bodies, and blood vessels. Although CAO works well in shallow regions of scattering mouse brain tissue, its performance degrades with distance from focus and overall imaging depth. Furthermore, unlike hardware wavefront shaping, which results in increased photon collection at the time of data acquisition, CAO cannot solve the fundamental problem of away-from-focus signal loss caused by confocal gating. The performance of CAO is also degraded by additional corruption from multiple scattering and cross talk. Further study is needed to investigate the factors limiting the performance of computational methods in scattering tissue, and potential approaches to mitigate these factors. Future work will also attempt to address motion artifacts, in order to achieve the phase stability required for *in-vivo* volumetric CAO-OCM in the scattering mouse brain.

6 Appendix

Figures 10–12 and Figs. 16–21 in this appendix are representative of videos that provide visualization of the CAO optimization process at selected depths below the surface of mouse brain. Figures 13–15 are representative of videos showing the sensitivity of the frequency metric to physical shifts of the optical focus. Figure 22 is representative of a video that provides a visualization of at-focus "ground truth" OCM, CAO-OCM, and OCM across all depths.

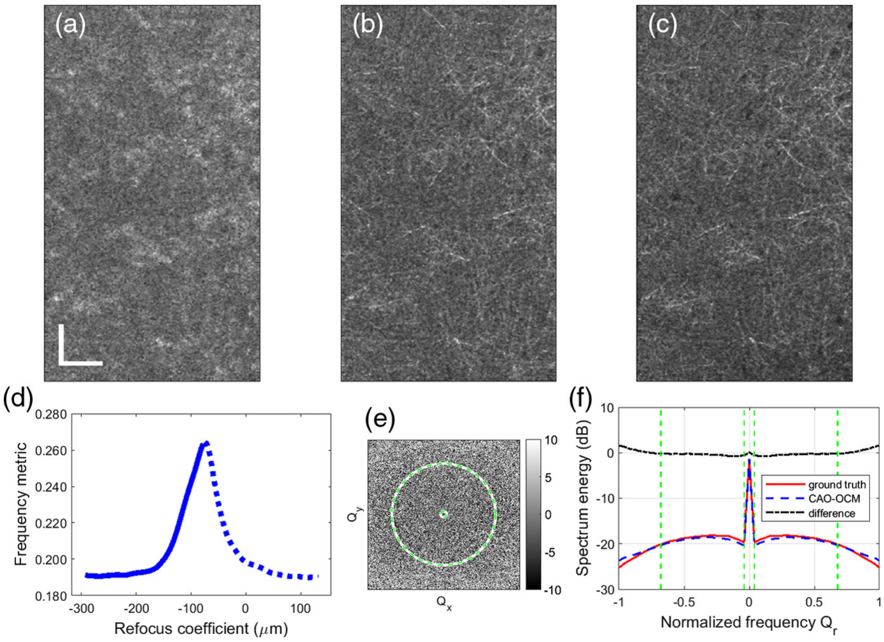

Fig. 10 Exhaustive search of refocus coefficient for plane at 44 μm OPL depth, with focus at 124 μm OPL depth. (a) OCM. (b) CAO-OCM with the optimal refocus coefficient from the frequency metric versus refocus coefficient curve in (d). (c) At-focus ground truth. (d) Plot of metric versus refocus coefficients. (e) Difference between spectrum energy of the magnitude of (c) ground truth and (b) CAO-OCM (in decibel scale). Here Q_x and Q_y are the transverse spatial frequency coordinates. (f) Plot of spectrum energy of magnitude of (c) ground truth and (b) CAO-OCM along normalized frequency radius axis Q_r. Green dash lines and green circles in (e) indicate the cut-off frequencies used for calculating frequency metric. Gamma correction was applied to the images with $\gamma = 0.7$. Scale bar = 100 μm (Video 1, MPEG, 11.7 MB [URL: https://doi.org/10.1117/1.JBO.24.11.116002.1]).

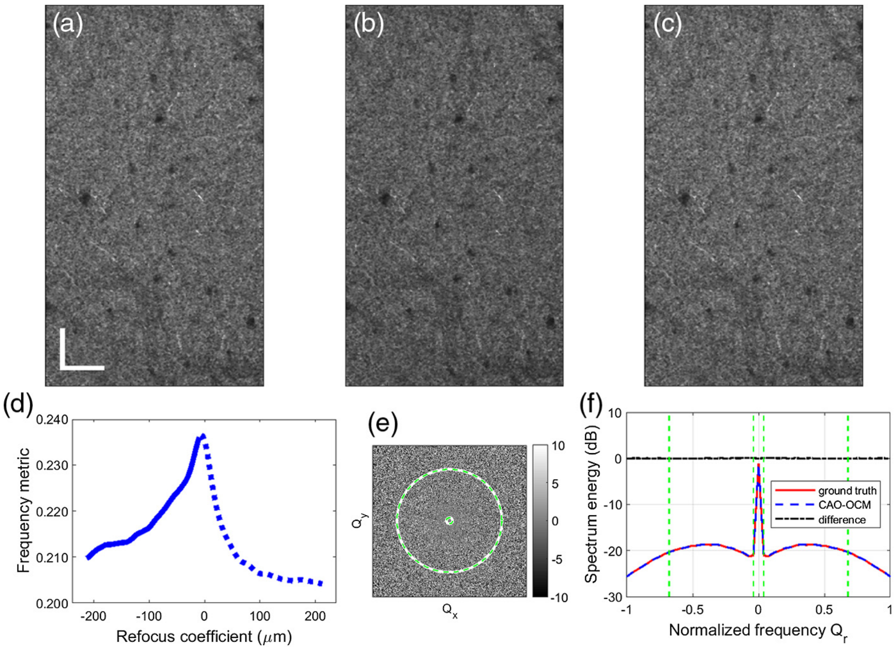

Fig. 11 Exhaustive search of refocus coefficient for plane at 125 μm OPL depth, with focus at 124 μm OPL depth. (a) OCM. (b) CAO-OCM with refocus coefficients corresponding to (d). (c) At-focus ground truth. (d) Plot of metric versus refocus coefficients. (e) Difference between spectrum energy of the magnitude of (c) ground truth and (b) CAO-OCM (in decibel scale). Here Q_x and Q_y are the transverse spatial frequency coordinates. (f) Plot of spectrum energy of magnitude of (c) ground truth and (b) CAO-OCM along normalized frequency radius axis Q_r. Green dash lines and green circles in (e) indicate the cut-off frequencies used for calculating frequency metric. Gamma correction was applied to the images with $\gamma = 0.7$. Scale bar = 100 μm (Video 2, MPEG, 11.8 MB [URL: https://doi.org/10.1117/1.JBO.24.11.116002.2]).

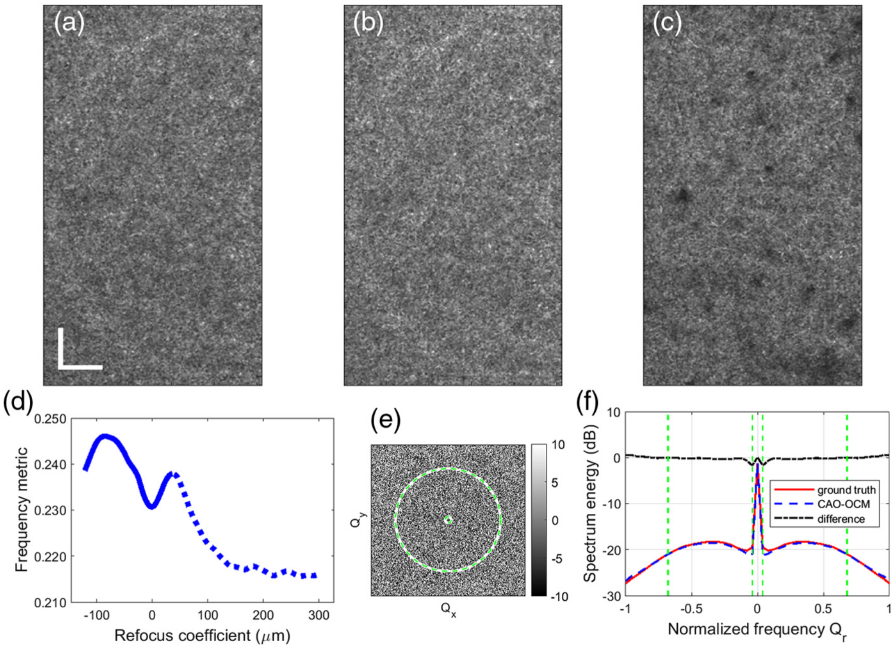

Fig. 12 Exhaustive search of refocus coefficient for plane at 215 μm OPL depth, with focus at 124 μm OPL depth. (a) OCM. (b) CAO-OCM with refocus coefficients corresponding to (d). (c) At-focus ground. (d) Plot of metric versus refocus coefficients. (e) Difference between spectrum energy of the magnitude of (c) ground truth and (b) CAO-OCM (in decibel scale). Here Q_x and Q_y are the transverse spatial frequency coordinates. (f) Plot of spectrum energy of magnitude of (c) ground truth and (b) CAO-OCM along normalized frequency radius axis Q_r. Green dash lines and green circles in (e) indicate the cut-off frequencies used for calculating frequency metric. Gamma correction was applied to the images with $\gamma = 0.7$. Scale bar = 100 μm (Video 3, MPEG, 10.4 MB [URL: https://doi.org/10.1117/1.JBO.24.11.116002.3]).

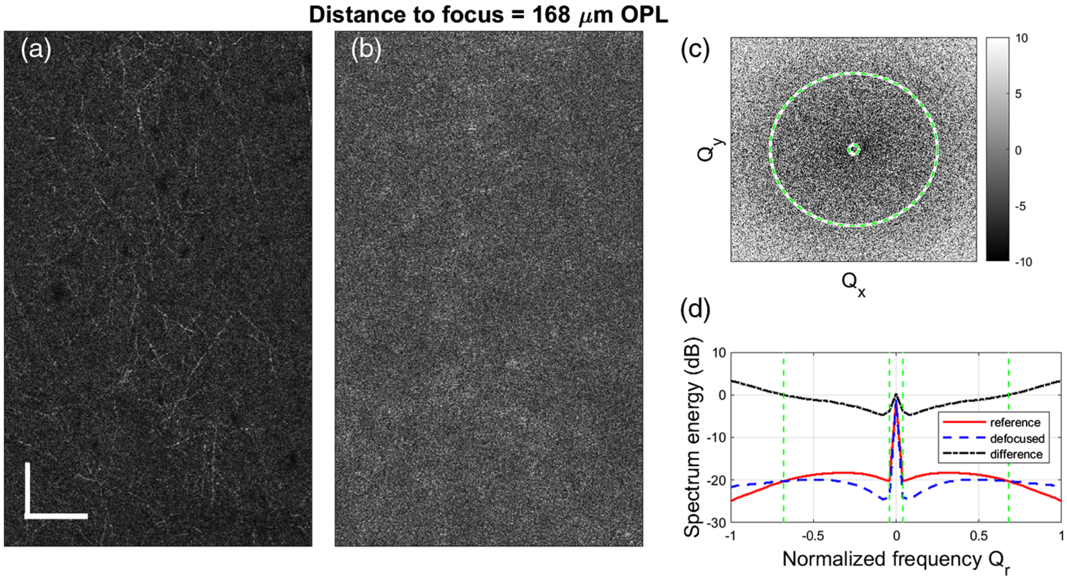

Fig. 13 Variations in transverse spectrum energy distribution of physically defocused images. (a) At-focus reference image at 94 μm OPL depth and (b) its defocused version, which is 168 μm above the focus (positive distance indicates depth above the focus, and negative distance indicates depth below the focus). (c) Difference between spectrum energy of the magnitude of reference image and defocused version (in decibel scale). Here Q_x and Q_y are the transverse spatial frequency coordinates. (d) Plot of spectrum energy of magnitude of reference and defocus version, and the difference between them (defocused version minus reference), along normalized frequency radius axis Q_r. Green dash lines and green circles in (c) and (d) indicate the cut-off frequencies used for calculating metrics Gamma correction was applied to the images with $\gamma = 0.7$. Scale bar = 100 μm. (Video 4, MPEG, 2.7 MB [URL: https://doi.org/10.1117/1.JBO.24.11.116002.4]).

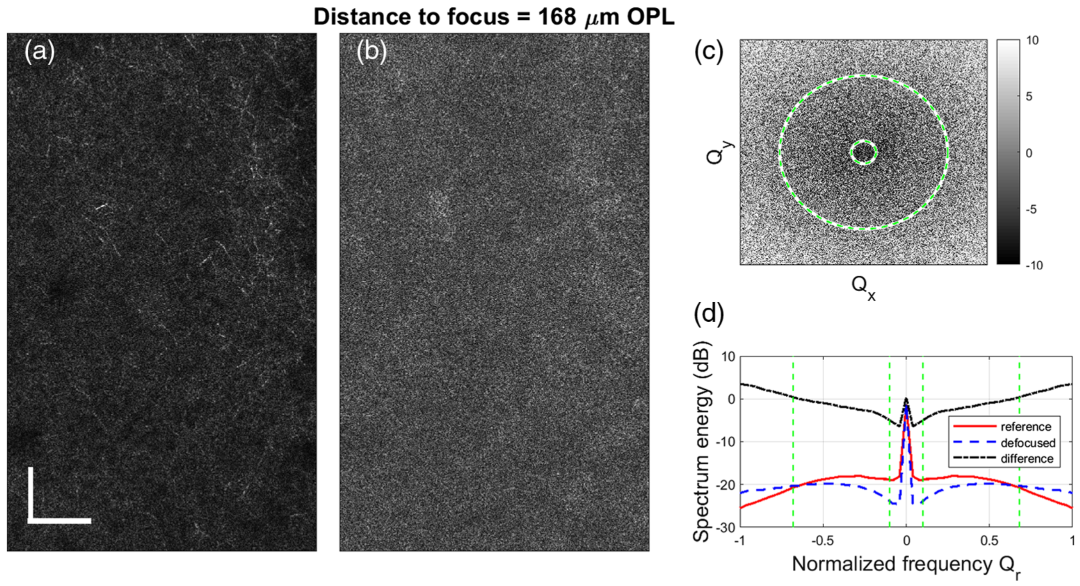

Fig. 14 Variations in transverse spectrum energy distribution of physically defocused images. (a) At-focus reference at 513 μm OPL depth and (b) its defocused version (positive distance indicates depth above the focus; negative distance indicates depth below the focus). (c) Difference between spectrum energy of the magnitude of reference and defocused version (in decibel scale). Here Q_x and Q_y are the transverse spatial frequency coordinates. (d) Plot of spectrum energy of magnitude of reference and defocus version, and the difference between them (defocused version minus reference), along normalized frequency radius axis Q_r. Green dash lines and green circles in (c) and (d) indicate the cut-off frequencies used for calculating metrics. Gamma correction was applied to the images with $\gamma = 0.7$. Scale bar = 100 μm (Video 5, MPEG, 3.2 MB [URL: https://doi.org/10.1117/1.JBO.24.11.116002.5]).

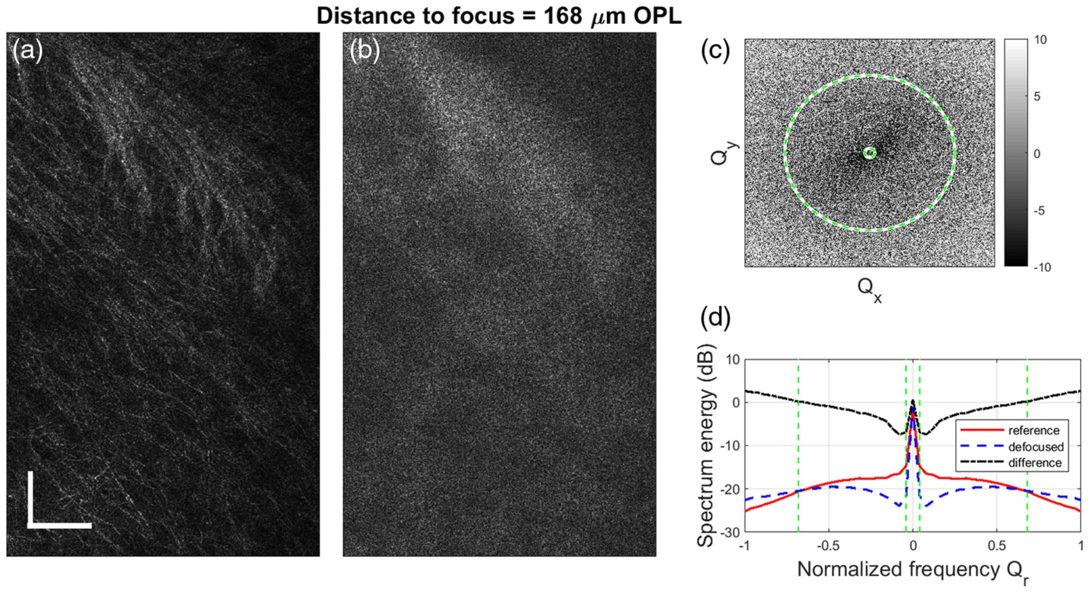

Fig. 15 Variations in transverse spectrum energy distribution of physically defocused images. (a) At-focus reference at 932 μm OPL depth and (b) its defocused versions (positive distance indicates depth above the focus; negative distance indicates depth below the focus). (c) Difference between spectrum energy of the magnitude of reference and defocused version (in decibel scale). Here Q_x and Q_y are the transverse spatial frequency coordinates. (d) Plot of spectrum energy of magnitude of reference and defocus version, and the difference between them (defocused version minus reference), along normalized frequency radius axis Q_r. Green dash lines and green circles in (c) and (d) indicate the cut-off frequencies used for calculating metrics. Gamma correction was applied to the images with $\gamma = 0.7$. Scale bar = 100 μm (Video 6, MPEG, 3.0 MB [URL: https://doi.org/10.1117/1.JBO.24.11.116002.6]).

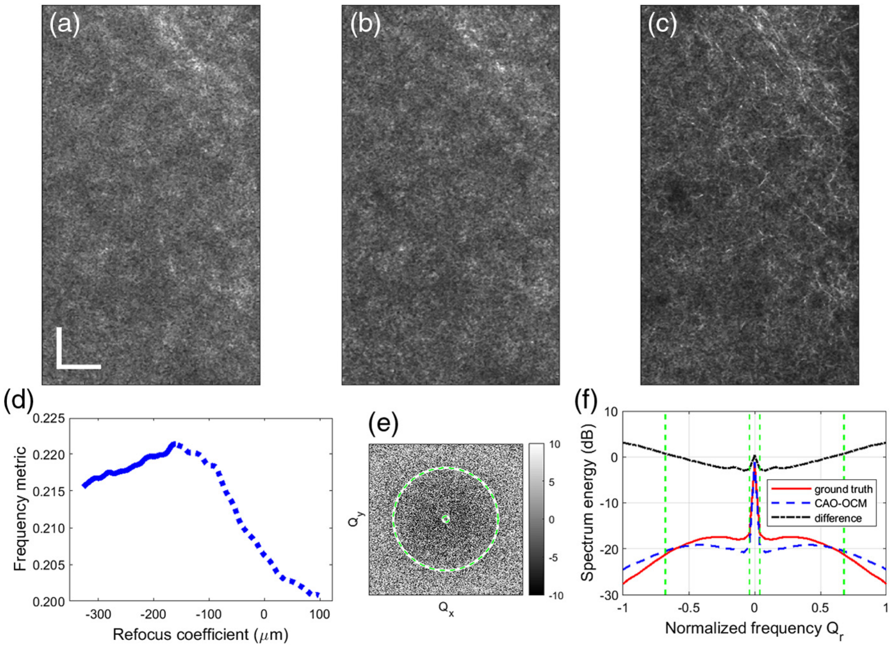

Fig. 16 Exhaustive search of refocus coefficient for plane at 609 μm OPL depth, with focus at 722 μm OPL depth. (a) OCM. (b) CAO-OCM with refocus coefficients corresponding to (d). (c) At-focus ground truth. (d) Plot of metric versus refocus coefficients. (e) Difference between spectrum energy of the magnitude of (c) ground truth and (b) CAO-OCM (in decibel scale). Here Q_x and Q_y are the transverse spatial frequency coordinates. (f) Plot of spectrum energy of magnitude of (c) ground truth and (b) CAO-OCM along normalized frequency radius axis Q_r. Green dash lines and green circles in (e) indicate the cut-off frequencies used for calculating frequency metric. Gamma correction was applied to the images with $\gamma = 0.7$. Scale bar = 100 μm (Video 7, MPEG, 11.5 MB [URL: https://doi.org/10.1117/1.JBO.24.11.116002.7]).

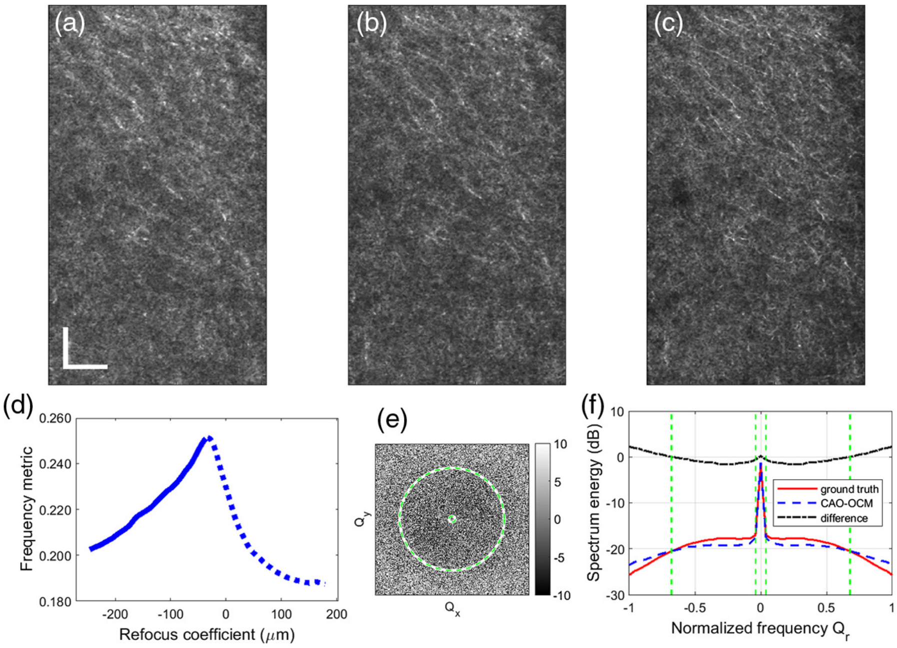

Fig. 17 Exhaustive search of refocus coefficient for plane at 690 μm OPL depth, with focus at 722 μm OPL depth. (a) OCM. (b) CAO-OCM with refocus coefficients corresponding to (d). (c) At-focus ground truth. (d) Plot metric versus refocus coefficients. (e) Difference between spectrum energy of the magnitude of (c) ground truth and (b) CAO-OCM (in decibel scale). Here Q_x and Q_y are the transverse spatial frequency coordinates. (f) Plot of spectrum energy of magnitude of (c) ground truth and (b) CAO-OCM along normalized frequency radius axis Q_r. Green dash lines and green circles in (e) indicate the cut-off frequencies used for calculating frequency metric. Gamma correction was applied to the images with $\gamma = 0.7$. Scale bar = 100 μm (Video 8, MPEG, 11.6 MB [URL: https://doi.org/10.1117/1.JBO.24.11.116002.8]).

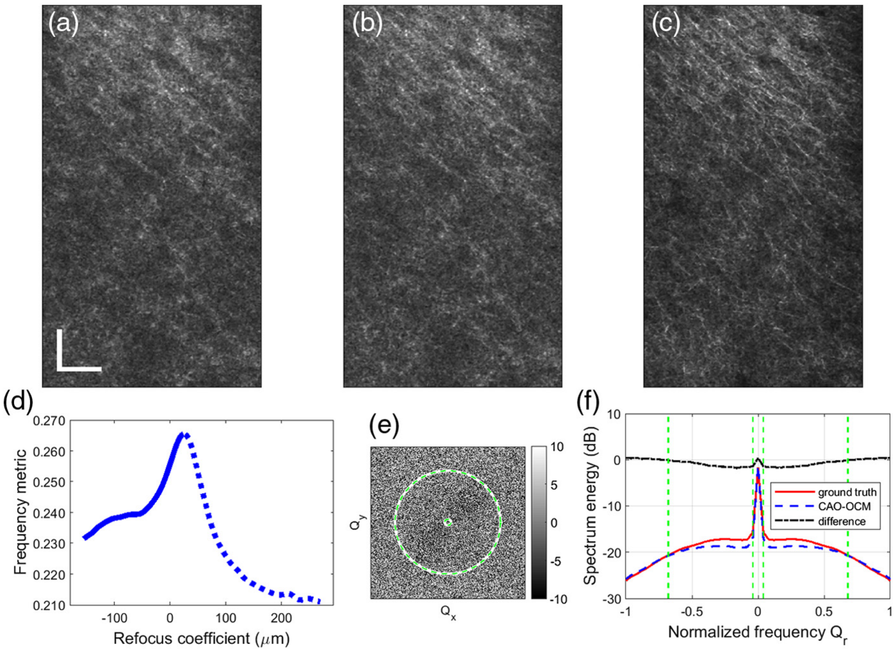

Fig. 18 Exhaustive search of refocus coefficient for plane at 781 μm OPL depth, with focus at 722 μm OPL depth. (a) OCM. (b) CAO-OCM with refocus coefficients corresponding to (d). (c) At-focus ground truth. (d) Plot of metric versus refocus coefficients. (e) Difference between spectrum energy of the magnitude of (c) ground truth and (b) CAO-OCM (in decibel scale). Here Q_x and Q_y are the transverse spatial frequency coordinates. (f) Plot of spectrum energy of magnitude of (c) ground truth and (b) CAO-OCM along normalized frequency radius axis Q_r. Green dash lines and green circles in (e) indicate the cut-off frequencies used for calculating frequency metric. Gamma correction was applied to the images with $\gamma = 0.7$. Scale bar = 100 μm (Video 9, MPEG, 11.2 MB [URL: https://doi.org/10.1117/1.JBO.24.11.116002.9]).

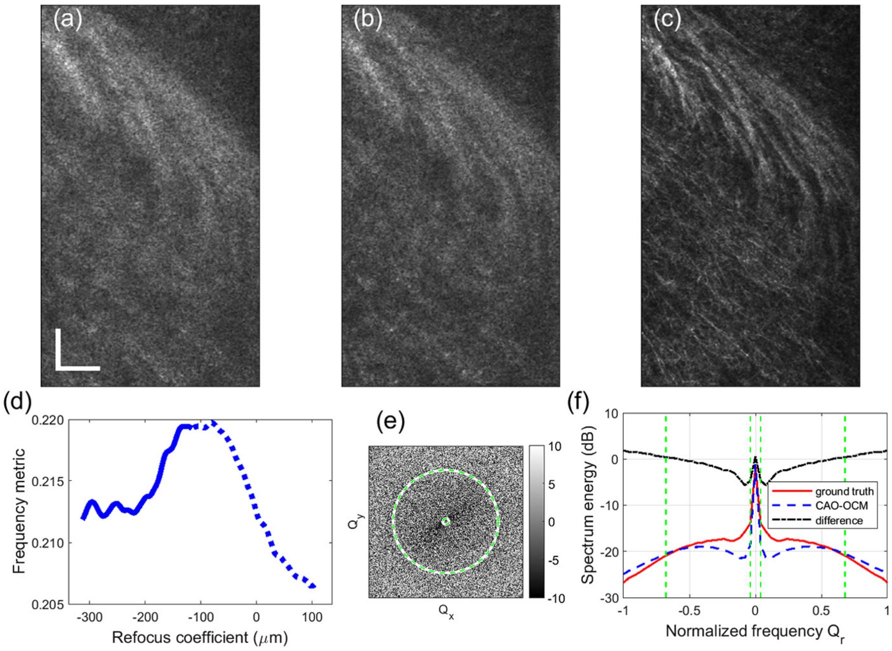

Fig. 19 Exhaustive search of refocus coefficient for plane at 980 μm OPL depth, with focus at 1082 μm OPL depth. (a) OCM. (b) CAO-OCM with refocus coefficients corresponding to (d). (c) At-focus ground truth. (d) Plot of metric versus refocus coefficients. (e) Difference between spectrum energy of the magnitude of (c) ground truth and (b) CAO-OCM (in decibel scale). Here Q_x and Q_y are the transverse spatial frequency coordinates. (f) Plot of spectrum energy of magnitude of (c) ground truth and (b) CAO-OCM along normalized frequency radius axis Q_r. Green dash lines and green circles in (e) indicate the cut-off frequencies used for calculating frequency metric. Gamma correction was applied to the images with $\gamma = 0.7$. Scale bar = 100 μm (Video 10, MPEG, 11.0 MB [URL: https://doi.org/10.1117/1.JBO.24.11.116002.10]).

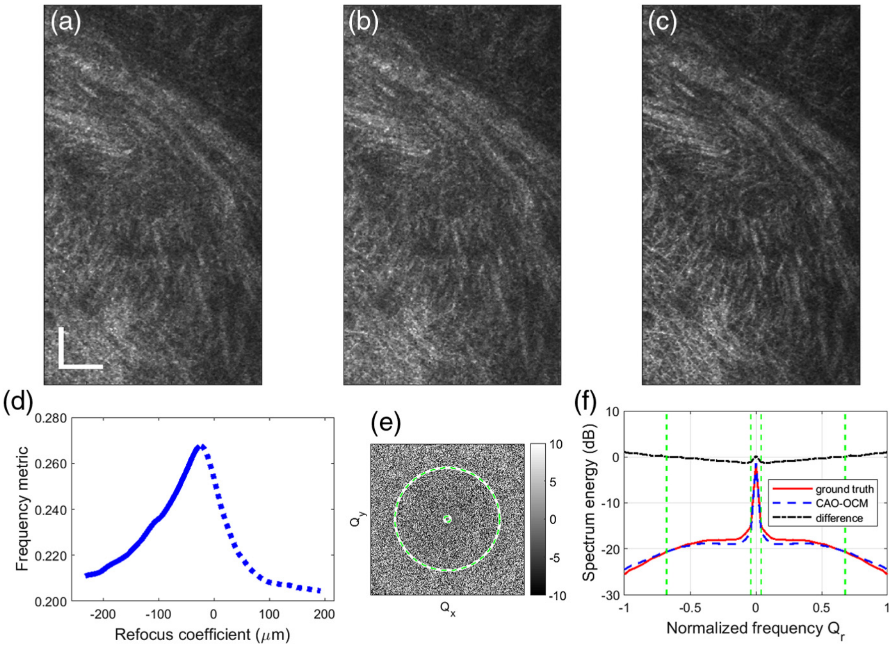

Fig. 20 Exhaustive search of refocus coefficient for plane at 1060 μm OPL depth, with focus at 1082 μm OPL depth. (a) OCM. (b) CAO-OCM with refocus coefficients corresponding to (d). (c) At-focus ground truth. (d) Plot of metric versus refocus coefficients. (e) Difference between spectrum energy of the magnitude of (c) ground truth and (b) CAO-OCM (in decibel scale). Here Q_x and Q_y are the transverse spatial frequency coordinates. (f) Plot of spectrum energy of magnitude of (c) ground truth and (b) CAO-OCM along normalized frequency radius axis Q_r. Green dash lines and green circles in (e) indicate the cut-off frequencies used for calculating frequency metric. Gamma correction was applied to the images with $\gamma = 0.7$. Scale bar = 100 μm (Video 11, MPEG, 11.0 MB [URL: https://doi.org/10.1117/1.JBO.24.11.116002.11]).

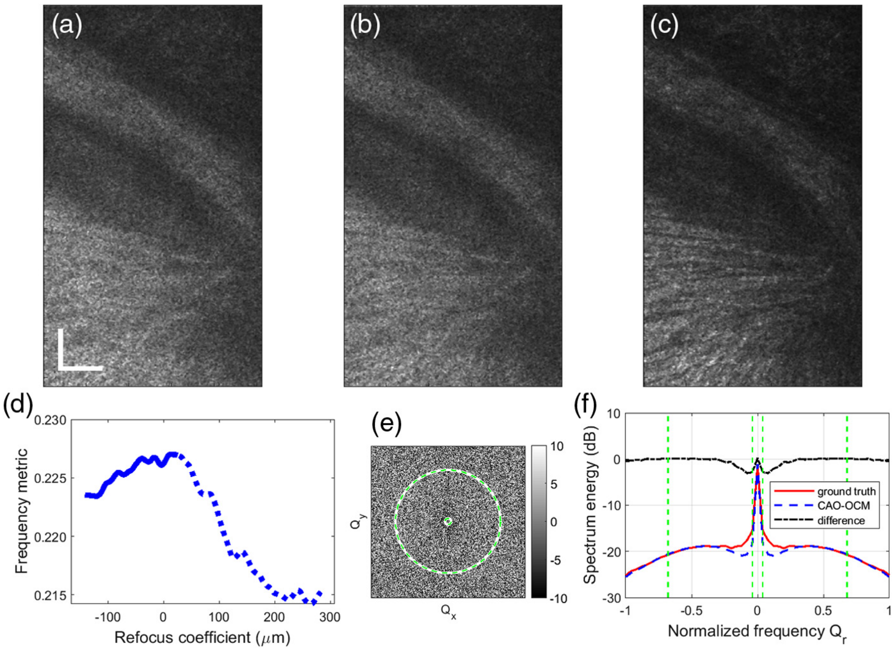

Fig. 21 Exhaustive search of refocus coefficient for plane at 1151 μm OPL depth, with focus at 1082 μm OPL depth. (a) OCM. (b) CAO-OCM with refocus coefficients corresponding to (d). (c) At-focus ground truth. (d) Plot of metric versus refocus coefficients. (e) Difference between spectrum energy of the magnitude of (c) ground truth and (b) CAO-OCM (in decibel scale). Here Q_x and Q_y are the transverse spatial frequency coordinates. (f) Plot of spectrum energy of magnitude of (c) ground truth and (b) CAO-OCM along normalized frequency radius axis Q_r. Green dash lines and green circles in (e) indicate the cut-off frequencies used for calculating frequency metric. Gamma correction was applied to the images with $\gamma = 0.7$. Scale bar = 100 μm (Video 12, MPEG, 10.4 MB [URL: https://doi.org/10.1117/1.JBO.24.11.116002.12]).

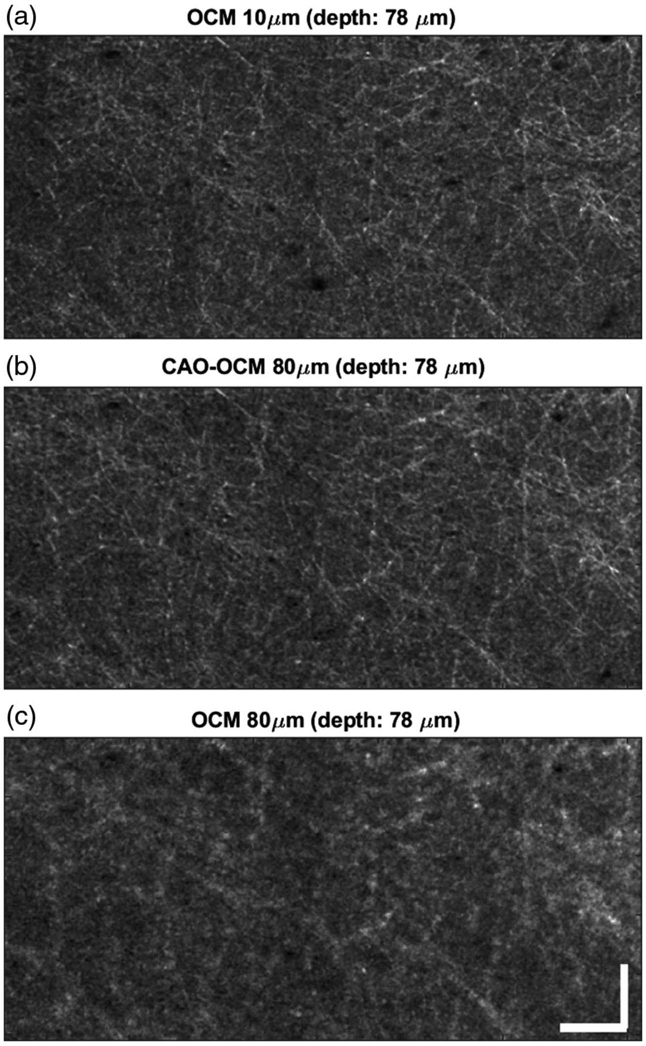

Fig. 22 Fly-through of (a) OCM with 10-μm focus spacing, (b) CAO-OCM with 80-μm focus spacing, and (c) OCM with 80-μm focus spacing. Each frame is a maximum project of 6 μm along depth. Images of CAO-OCM and OCM are histogram equalized to the histogram of ground truth. Gamma correction was applied to the images with $\gamma = 0.8$. Scale bar = 100 μm (Video 13, MPEG 11.7 MB [URL: https://doi.org/10.1117/1.JBO.24.11.116002.13]).

Disclosures

The authors have no relevant financial interests in the article and no other potential conflicts of interest to disclose.

Acknowledgments

This research was supported by the National Science Foundation (CAREER: CBET-1752405) and National Institutes of Health (No. 1R21EY028389).

References

1. V. J. Srinivasan et al., "Optical coherence microscopy for deep tissue imaging of the cerebral cortex with intrinsic contrast," *Opt. Express* **20**(3), 2220–2239 (2012).
2. B. J. Vakoc et al., "Three-dimensional microscopy of the tumor microenvironment *in vivo* using optical frequency domain imaging," *Nat. Med.* **15**(10), 1219–1223 (2009).
3. W. J. Choi and R. K. Wang, "Swept-source optical coherence tomography powered by a 1.3-μm vertical cavity surface emitting laser enables 2.3-mm-deep brain imaging in mice *in vivo*," *J. Biomed. Opt.* **20**(10), 106004 (2015).
4. C. J. Goergen et al., "Optical coherence tractography using intrinsic contrast," *Opt. Lett.* **37**(18), 3882–3884 (2012).
5. J. Binding et al., "Brain refractive index measured *in vivo* with high-NA defocus-corrected full-field OCT and consequences for two-photon microscopy," *Opt. Express* **19**(6), 4833–4847 (2011).
6. S. G. Adie et al., "Computational adaptive optics for broadband optical interferometric tomography of biological tissue," *Proc. Natl. Acad. Sci. U. S. A.* **109**(19), 7175–7180 (2012).
7. A. Kumar, W. Drexler, and R. A. Leitgeb, "Subaperture correlation based digital adaptive optics for full field optical coherence tomography," *Opt. Express* **21**(9), 10850–10866 (2013).
8. S. G. Adie et al., "Guide-star-based computational adaptive optics for broadband interferometric tomography," *Appl. Phys. Lett.* **101**(22), 221117 (2012).
9. N. D. Shemonski et al., "Computational high-resolution optical imaging of the living human retina," *Nat. Photonics* **9**(7), 440–443 (2015).
10. L. Ginner et al., "Noniterative digital aberration correction for cellular resolution retinal optical coherence tomography *in vivo*," *Optica* **4**(8), 924–931 (2017).
11. D. Hillmann et al., "Aberration-free volumetric high-speed imaging of *in vivo* retina," *Sci. Rep.* **6**, 35209 (2016).
12. C. Blatter et al., "Extended focus high-speed swept source OCT with self-reconstructive illumination," *Opt. Express* **19**(13), 12141–12155 (2011).
13. P. J. Marchand et al., "Visible spectrum extended-focus optical coherence microscopy for label-free sub-cellular tomography," *Biomed. Opt. Express* **8**(7), 3343–3359 (2017).
14. Y. Xu et al., "Multifocal interferometric synthetic aperture microscopy," *Opt. Express* **22**(13), 16606–16618 (2014).
15. T. S. Ralston et al., "Interferometric synthetic aperture microscopy," *Nat. Phys.* **3**(2), 129–134 (2007).
16. L. F. Yu et al., "Improved lateral resolution in optical coherence tomography by digital focusing using two-dimensional numerical diffraction method," *Opt. Express* **15**(12), 7634–7641 (2007).
17. Y. Yasuno et al., "Non-iterative numerical method for laterally superresolving Fourier domain optical coherence tomography," *Opt. Express* **14**(3), 1006–1020 (2006).
18. J. P. Rolland et al., "Gabor domain optical coherence microscopy," *Proc. SPIE* **7139**, 71390F (2009).
19. K.-S. Lee et al., "Three-dimensional imaging of normal skin and nonmelanoma skin cancer with cellular resolution using Gabor domain optical coherence microscopy," *J. Biomed. Opt.* **17**(12), 126006 (2012).
20. S. Jung et al., "Analysis of fractalkine receptor CX3CR1 function by targeted deletion and green fluorescent protein reporter gene insertion," *Mol. Cell. Biol.* **20**(11), 4106–4114 (2000).
21. G. Feng et al., "Imaging neuronal subsets in transgenic mice expressing multiple spectral variants of GFP," *Neuron* **28**(1), 41–51 (2000).
22. J. P. Rolland et al., "Gabor-based fusion technique for optical coherence microscopy," *Opt. Express* **18**(4), 3632–3642 (2010).
23. J. A. Mulligan, X. Feng, and S. G. Adie, "Quantitative reconstruction of time-varying 3D cell forces with traction force optical coherence microscopy," *Sci. Rep.* **9**(1), 4086 (2019).
24. T. S. Ralston et al., "Phase stability technique for inverse scattering in optical coherence tomography," in *3rd IEEE Int. Symp. Biomedical Imaging: Nano to Macro, 2006*, IEEE, pp. 578–581 (2006).
25. T. A. Pologruto, B. L. Sabatini, and K. Svoboda, "ScanImage: flexible software for operating laser scanning microscopes," *Biomed. Eng. Online* **2**(1), 13 (2003).
26. R. A. Hill, A. M. Li, and J. Grutzendler, "Lifelong cortical myelin plasticity and age-related degeneration in the live mammalian brain," *Nat. Neurosci.* **21**(5), 683–695 (2018).
27. M. J. Farrar et al., "In vivo imaging of myelin in the vertebrate central nervous system using third harmonic generation microscopy," *Biophys. J.* **100**(5), 1362–1371 (2011).
28. A. E. Tippie and J. R. Fienup, "Phase-error correction for multiple planes using a sharpness metric," *Opt. Lett.* **34**(5), 701–703 (2009).
29. M. Cua et al., "Coherence-gated sensorless adaptive optics multiphoton retinal imaging," *Sci. Rep.* **6**, 32223 (2016).
30. F. A. South et al., "Wavefront measurement using computational adaptive optics," *J. Opt. Soc. Am. A* **35**(3), 466–473 (2018).

31. F. A. South et al., "Local wavefront mapping in tissue using computational adaptive optics OCT," *Opt. Lett.* **44**(5), 1186–1189 (2019).
32. S. Liu, J. A. Mulligan, and S. G. Adie, "Volumetric optical coherence microscopy with a high space-bandwidth-time product enabled by hybrid adaptive optics," *Biomed. Opt. Express* **9**(7), 3137–3152 (2018).
33. A. F. Fercher et al., "Optical coherence tomography-principles and applications," *Rep. Prog. Phys.* **66**(2), 239–303 (2003).
34. B. Karamata et al., "Multiple scattering in optical coherence tomography. I. Investigation and modeling," *J. Opt. Soc. Am. A* **22**(7), 1369–1379 (2005).
35. D. Hillmann et al., "Efficient holoscopy image reconstruction," *Opt. Express* **20**(19), 21247–21263 (2012).
36. A. Badon et al., "Multiple scattering limit in optical microscopy," *Opt. Express* **25**(23), 28914–28934 (2017).
37. V. V. Tuchin, *Optical Clearing of Tissues and Blood*, SPIE Press, Bellingham, Washington (2006).
38. N. D. Shemonski et al., "Stability in computed optical interferometric tomography (part I): stability requirements," *Opt. Express* **22**(16), 19183–19197 (2014).
39. S. G. Adie et al., "Interferometric synthetic aperture microscopy (ISAM)," in *Optical Coherence Tomography: Technology and Applications*, W. Drexler and J. Fujimoto, Eds., pp. 965–1004, Springer, Cham (2015).
40. N. D. Shemonski et al., "Three-dimensional motion correction using speckle and phase for *in vivo* computed optical interferometric tomography," *Biomed. Opt. Express* **5**(12), 4131–4143 (2014).

Meiqi Wu is a PhD candidate at the Meinig School of Biomedical Engineering at Cornell University. She obtained her BS degree in electrical engineering from the University of Science and Technology of China. Her research in the group is on the development of computational and hardware adaptive optics approaches for optical coherence tomography (OCT)-based imaging in mouse brain.

David M. Small is a postdoctoral associate at the Meinig School of Biomedical Engineering, Cornell University. He received his PhD from the University of Queensland, Australia, where he investigated the role of oxidative stress in chronic renal pathologies using intravital imaging approaches. Currently, he specializes in applying multiphoton microscopy to the beating mouse heart to study cardiac function during health and disease.

Nozomi Nishimura is an associate professor at the Meinig School of Biomedical Engineering at Cornell University. Her PhD is in physics from the University of California at San Diego with Professor David Kleinfeld where she studied blood flow in the brain. Her postdoctoral work at Cornell was on neurodegenerative disease. Her current research develops optical tools for *in-vivo* physiology rodent studies in multiple organ systems.

Steven G. Adie is an associate professor at the Meinig School of Biomedical Engineering at Cornell University. After earning his PhD from the University of Western Australia, he conducted postdoctoral research at the University of Illinois at Urbana-Champaign. His interests include the development of OCT-based imaging techniques for the study of biophysical cell–extracellular matrix interactions in mechanobiology, and the integration of computational and hardware wavefront shaping methods for faster and deeper volumetric microscopy in scattering media.